Low-temperature phase transitions in the induced-moment system PrB_4

G. A. Wigger, E. Felder, R. Monnier, and H. R. Ott
Laboratorium für Festkörperphysik, ETH-Hönggerberg, CH-8093 Zürich, Switzerland

L. Pham and Z. Fisk
Department of Physics, University of California, Davis, California 95616, USA
(Received 10 January 2005; published 8 July 2005)

We report the results of measurements of the electrical resistivity, the magnetization, and the specific heat of PrB_4 below room temperature. The crystal electric field (CEF) splits the $4f^2$ multiplet of the Pr ions into nine singlets. In its ground state, PrB_4 is an induced-moment ferromagnet with a saturation magnetization as high as $2.1\mu_B$/(Pr ion). Contrary to previous experiments, we observe a first-order ferromagnetic to antiferromagnetic transition at $T_C \approx 15.9 \pm 0.1$ K with a latent heat $\Delta Q = 8.6$ J/mol. The antiferromagnetic long-range order is quenched above $T_N = 19.5$ K. Susceptibility and specific heat data, as well as the enormous magnetic anisotropy, can quantitatively be reproduced by a mean-field calculation which takes into account the CEF, obtained from a point-charge model using effective charges obtained from a self-consistent electronic band-structure calculation and a Zeeman term, as well as an anisotropic dipolar magnetic exchange and an effective quadrupole-quadrupole interaction term.

DOI: 10.1103/PhysRevB.72.014419 PACS number(s): 75.10.Dg, 75.30.Gw, 75.40.Cx

I. INTRODUCTION

Previous work, reporting on the low-temperature properties of rare-earth (RE) tetraborides (RB_4), revealed the occurrence of two subsequent phase transitions in some of the members of this series: namely, with R=Tb, Dy, Ho, and Tm.[1–3] This is particularly intriguing for those cases where the rare-earth ions are non-Kramers ions. The low symmetry of the RE sites provokes a complete lifting of the degeneracy of the Hund's-rule ground-state multiplet into singlet states by the crystal electric field (CEF), and thus, any phase transition may only be triggered by second-order effects. For instance, a magnetic phase transition requires a nonzero dipolar coupling of two singlets and the instability may then be induced by an overcritical exchange interaction.[4–6] In metals, such as these tetraborides, this interaction is mediated by conduction electrons.

Since we are not aware of any follow-up work discussing the above-mentioned experimental results in some detail, we present new results and their interpretation on low-temperature properties of PrB_4. The Pr ions adopt a $4f^2$ configuration and hence the corresponding Hund's-rule ground-state multiplet, with total angular momentum J=4, splits into nine singlet states under the influence of the CEF. Previous work on this compound reported a considerable anisotropy of the magnetic susceptibility below room temperature and the onset of ferromagnetic order at a Curie temperature of T_C=24 K.[7,8] Our experiments, probing the electrical resistivity, the magnetization, and the specific heat as a function of temperature and, at least partly, in external magnetic fields, reveal two zero-field phase transitions at 19.5 and 15.9 K, respectively. While the transition at 19.5 K exhibits the features of a second-order phase transition, the transition at 15.9 K is clearly of first order. Both transitions affect magnetic degrees of freedom. The mean-field-type calculations of the experimentally accessible quantities require the introduction of three fit parameters. Two of them relate to the anisotropic magnetic coupling, and the third captures the interaction between the electric quadrupoles on the Pr ions and elastic degrees of freedom.

In Sec. II, we briefly describe the sample, its synthesis, and the employed experimental methods. In Sec. III, we present the experimental results on the zero-field resistivity $\rho(T)$, the magnetoresistance at low temperatures in various fields up to 7 T, the low-field susceptibility $\chi(T)$, and the magnetization $M(H)$, as well as the specific heat $C_p(T)$ in zero field for temperatures between 0.4 and 30 K. Section IV is split into two parts. In Sec. IV A, we describe a point-charge evaluation of the CEF acting on the Pr ions, based on calculated ionic charges, and Sec. IV B contains a discussion of the total Hamiltonian describing the system, including the CEF term, the anisotropic magnetic exchange, and the (effective) quadrupole-quadrupole interaction. In Sec. V we calculate the thermodynamic properties which follow from the Hamiltonian of Sec. IV B and compare them with the experimental data. Conclusions are presented in Sec. VI.

II. SAMPLES AND EXPERIMENTS

The single-crystalline sample of PrB_4 was prepared by flux growth in a Ta crucible, using a flux with the composition $Pr_{0.75}Co_{0.25}$ and an amount of 0.1 PrB_4/(Pr/Co) in the melt. The growth was cooled from 1150 °C to 500 °C at a rate of approximately 35 °C/h. Single crystals of millimeter size were extracted from the solidified flux by dissolving it in HCl. X-ray checks[9] verified the tetragonal VB_4 structure reported in the literature.[10] The lattice parameters are in close agreement with those published previously.[8] All experiments were made using the same single crystal in the form of a platelet with dimensions of $4.25 \times 4.2 \times 0.05$ mm^3. The x-ray Laue diffraction image in Fig. 1 shows that the c axis is orthogonal to the platelet. For the electronic transport mea-

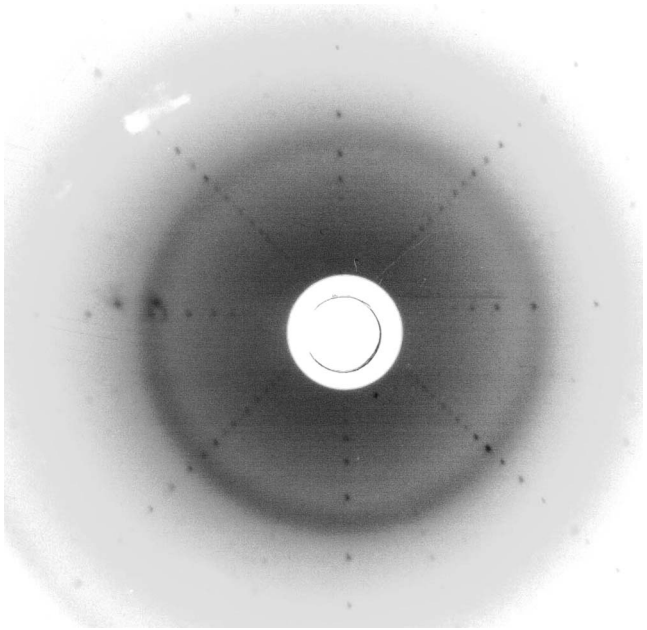

FIG. 1. X-ray Laue diffraction image of our PrB_4 sample. The platelet plane was oriented perpendicularly to the x-ray beam.

surements, gold wires with 50 μm diameter were attached to the sample with silver epoxy. All voltages were measured with a four-probe, low-frequency ac technique in the Ohmic regime. The transverse magnetoresistance, in the following always referred to as the magnetoresistance, was measured in a configuration where the external field H, between 0 and 7 T, was oriented perpendicular to both the applied current and the measured voltages, thus orthogonal to the platelet plane. The extended temperature range was covered by using a conventional ^{4}He cryostat and a homebuilt ^{3}He system. Magnetization measurements for H orthogonal and parallel to the platelet plane were made with a commercial superconducting quantum interference device (SQUID) magnetometer, for temperatures between 2 and 330 K and magnetic fields up to 5.5 T. The specific heat $C_p(T)$ was measured in the temperature range between 0.4 and 30 K with a conventional relaxation-type method. A sapphire disk onto which a heater had been evaporated and a Ru-oxide thermometer had been glued with EPO-TEK H20E was weakly thermally coupled to a heat sink which could be held at constant temperature. The platelet-shaped sample was mounted on the sapphire disk using a thin layer of Apiezon grease.

III. EXPERIMENTAL RESULTS

In Fig. 2, the resistivity $\rho(T)$ of PrB_4 is plotted for temperatures between 0.4 and 300 K. We note an overall metallic conduction, nearly linear in T above 50 K. Below 25 K, an abrupt change in $\rho(T)$ with a maximum slope at $T_C \approx 15.9$ K indicates a phase transition. The magnetoresistance shown in the inset of Fig. 2 is negative above 16 K and most likely due to the reduction of spin-disorder scattering. The positive magnetoresistance below the transition reflects the fact that carriers from more than one electronic energy band are involved in the charge transport.

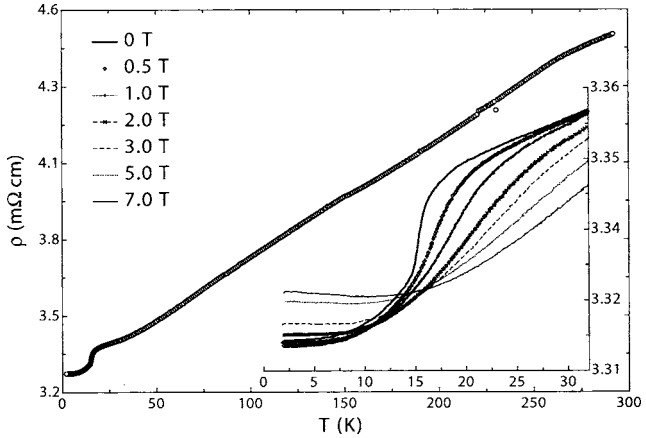

FIG. 2. Electrical resistivity $\rho(T)$ for PrB_4 between 0.4 and 290 K. The inset shows $\rho(T)$ at low temperatures for various external magnetic fields H, as indicated in the main frame.

In Fig. 3, we present the magnetic susceptibility $\chi(T) = M(H,T)/H$ for $\vec{H}$ parallel and orthogonal to the c axis, denoted as $\chi_\parallel$ and $\chi_\perp$, respectively. The susceptibility $\chi_\parallel$, measured for $H=50$ Oe (open circles) and =1 kOe (solid circles), clearly reveals two magnetic phase transitions. The upper anomaly indicates a second-order magnetic transition into an antiferromagnetic state below $T_N \sim 19.5$ K. The lower transition is of first order and to a ferromagnetic ground state below $T_C \sim 15.9$ K. At low temperatures, the susceptibility $\chi_\perp$ is two orders of magnitude smaller than $\chi_\parallel$, which reflects the influence of the strong crystal electric field. In the inset of Fig. 3, we display $M(H)$ for $T=2$ K. For $H>5$ kOe, the magnetic moment saturates at a saturation magnetization $\mu_{sat} \approx 2.1 \mu_B$/(Pr ion). A small magnetic hysteresis is observed for $H<5$ kOe, as indicated by the solid arrows. The strong decrease of $\chi_{parallel}(T)$ observed at the low end of the covered temperature range in fields of a few hundred Oersteds is most likely due to domain effects.

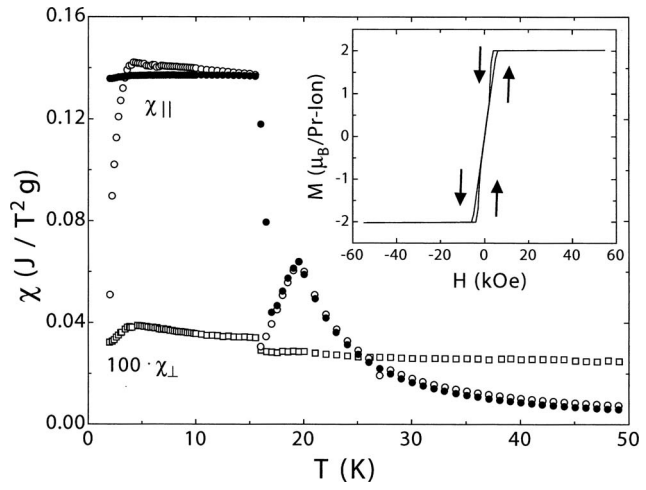

FIG. 3. The magnetic susceptibility $\chi_\parallel(T)$ for PrB_4 for H =50 Oe (open circles) and=1 kOe (solid circles) and oriented parallel to the c axis. For $H=1$ kOe and perpendicular to the c axis, $100\chi_\perp(T)$ is displayed as open squares. The inset emphasizes $M(H)$ at 2 K. The arrows indicate the direction of the field variation.

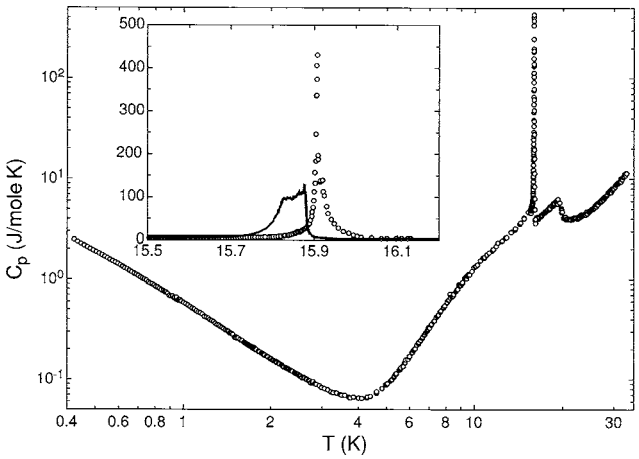

FIG. 4. Specific heat $C_p(T)$ for PrB_4 in zero magnetic field below 30 K. The inset highlights the first-order character of the phase transition. The open circles and the black dots denote $C_p(T)$ measured upon warming and cooling, respectively.

In Fig. 4, the specific heat $C_p(T)$ of PrB_4 in zero applied field is plotted for temperatures between 0.4 and 30 K. For $T<4$ K, $C_p(T)$ exhibits a nearly inverse quadratic dependence on temperature, indicating the presence of a Schottky anomaly due to nuclear degrees of freedom. The two magnetic phase transitions indicated in the $\chi(T)$ data are also reflected in $C_p(T)$ at the same temperatures $T_N \sim 19.5$ K and $T_C \sim 15.9$ K for the second-order and first-order transitions, respectively. The inset of Fig. 4 highlights the hysteresis of the specific heat upon cooling (black dots) and heating (open circles). We observe a supercooling-superheating effect of the order of 100 mK. The latent heat, obtained from integrating $[C_p(T)/T]T_C$ in the critical temperature regime around T_C, is $\Delta Q \approx 8.6$ J/mol $[\approx 0.09R \ln(2)T_C]$.

IV. MODEL ASSUMPTIONS AND CALCULATIONS

A. Crystal structure and crystal electric field

As can be inferred from Fig. 5(a), PrB_4 crystallizes in the tetragonal VB_4 structure,[10] space group D_4^5h. The boron sublattice consists of chains of B octahedra parallel to the c axis and connected by B_2 barbells. The resulting three-dimensional skeleton contains tunnels along the c axis which are filled with Pr ions. Figure 5(b) provides a view along these tunnels. The low symmetry of the space group is the reason for extremely anisotropic magnetic and electrical properties in various tetraboride systems.[11]

In very early work, Lipscomb and Britton claimed that the stability of the boron sublattice requires the transfer of an electron from the metal cation to the B_4 sublattice.[12] Much later, crystal electric field effects were investigated by Kasaya *et al.*[13] on the basis of a point-charge model assuming trivalent Pr^{3+} and B_4^{3-} ions. Their calculation confirmed the splitting of the ninefold-degenerate $^3H_4$ multiplet of the Pr ions into nine singlets, as expected from the low structural symmetry. However, according to the authors the resulting splitting has to be reduced by at least a factor of 2 in order to reproduce their experimental $M(H)$ and $\rho(T)$ data.

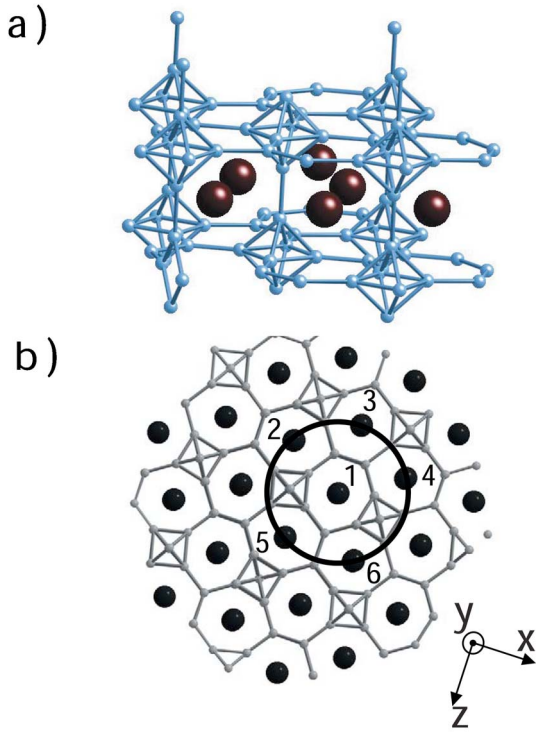

FIG. 5. (Color online) Panels (a) and b) model the crystal structure of PrB_4 from an arbitrary solid angle and in the ab plane, respectively. The larger balls denote the Pr ions, the smaller the B ions, respectively.

In the present work, the coordinates of the 20 ions in the unit cell of Pr_4B_{16} were optimized to match the experimental lattice parameters $a=b=7.235$ Å and $c=4.116$ Å,[8] using the self-consistent electronic structure code (DMol^3) developed by Delley,[14] which yielded effective (Mulliken) charges at the ionic sites.[15] These results are summarized in Table I. Note that the calculated ionic charges are vastly different from the usually employed nominal valences of the ions. With these parameters, the CEF at the Pr site can be computed under the assumption that intra-atomic contributions are negligible. The local symmetry at the Pr sites is C_{2v}. A natural choice of the coordinate system is sketched in Fig. 5(b). At site Pr-1, the negative z direction points towards Pr-3. To each of the four inequivalent Pr sites (1, 2, 3, and 4) we assign a different coordinate system, distinguished by successive rotations of $\pi/2$ around the c axis. Sites 5 and 6 in the figure are equivalent to sites 4 and 2, respectively. At the position $\vec{r}$ measured from $\vec{R}_i$, the Coulomb potential close to ion i, caused by the surrounding charges, is given by

$$V(\vec{r}) = \frac{1}{4\pi\epsilon_0} \sum_{j \neq i} \frac{q_j}{|\vec{R}_j - \vec{r}|}. \quad (1)$$

The index j includes all considered Pr and B sites except site i. In order to achieve convergence of the sum in Eq. (1), we had to include all charged ions within a radius of 15 Å from the chosen Pr ion. It is assumed that the $4f$-electron orbitals do not overlap with orbitals of the neighboring ions, so that, for $|\vec{r}|<3$ Å, $V(\vec{r})$ satisfies Laplace's equation and

TABLE I. Optimized internal coordinates (in units of the cell parameters) and Mulliken charges for the 20 ions in the unit cell of PrB_4.

Atom	x^*	y^*	z^*	Q [$\|e\|$]
Pr	0.315	−0.185	0	0.466
Pr	−0.315	0.185	0	0.466
Pr	0.185	0.315	0	0.466
Pr	−0.185	−0.315	0	0.466
B	−0.088	0.411	0.5	−0.118
B	0.088	−0.411	0.5	−0.118
B	0.411	0.088	0.5	−0.118
B	−0.411	−0.088	0.5	−0.118
B	0	0	0.203	−0.153
B	0	0	−0.203	−0.153
B	0.5	0.5	0.203	−0.153
B	0.5	0.5	−0.203	−0.153
B	0.175	0.038	0.5	−0.098
B	−0.175	−0.038	0.5	−0.098
B	0.325	0.462	0.5	−0.098
B	−0.325	−0.462	0.5	−0.098
B	−0.038	0.175	0.5	−0.098
B	0.038	−0.175	0.5	−0.098
B	0.462	0.325	0.5	−0.098
B	−0.462	−0.325	0.5	−0.098

can be expanded in spherical harmonics according to

$$V(\vec{r}) = \sum_{l} \sum_{m=-l}^{+l} A_{l,m} r^l Y_{l,m}(\theta,\phi), \tag{2}$$

where $\vec{r}=|r|(\sin\theta\cos\phi, \sin\theta\sin\phi, \cos\theta)$ and $|r|$ is the distance to the ion i. The C_{2v} symmetry allows nonvanishing coefficients only for $l=2$, 4, and 6 and for even m. The coefficients $A_{l,m}$ are related to the coefficients of the Stevens operator equivalents by[16]

$$B_{l,m} = \langle r^l \rangle \xi_l A_{l,m}, \tag{3}$$

with

$$\xi_2 = \alpha = -\frac{2\times 13}{3^2\times 5^2\times 11},$$

$$\xi_4 = \beta = -\frac{2^2}{3^2\times 5\times 11^2},$$

$$\xi_6 = \gamma = -\frac{2^4\times 17}{3^4\times 5\times 7\times 11^2\times 13}. \tag{4}$$

On the basis of the theoretical results obtained by Liu *et al.* for other Pr-based alloys,[17] the values for $\langle r^l \rangle$ are taken as 1.45, 8, and 150 in units of the Bohr radius to the power l for $l=2$, 4, and 6. Hence, the CEF Hamiltonian is written as

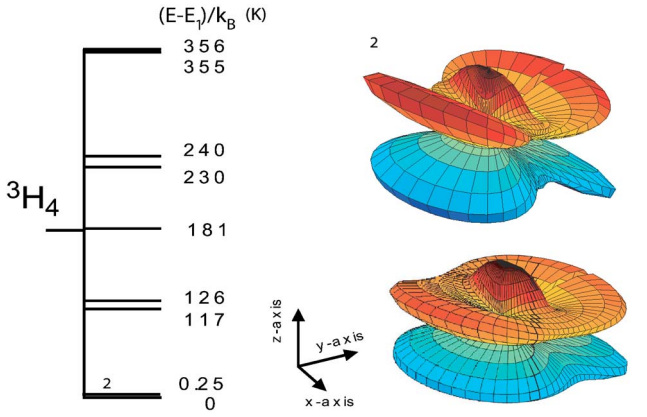

FIG. 6. (Color online) The left side shows the CEF splitting of the $4f^2$ multiplet in PrB_4 due to H_{CEF} (see text). The right side pictures the orbitals for the two lowest levels, denoted as 1 and 2. The gap in the orbital pictures is an artifact of the computer program.

$$\mathcal{H}_{CEF} = \sum_{l,m} B_{l,m} \mathcal{O}_l^m, \tag{5}$$

where the $\mathcal{O}_l^m$ denote the Stevens operator equivalents.[18] The energy level scheme, emerging from the CEF splitting of the $J=4$ Hund's-rule ground state multiplet is shown in the left part of Fig. 6. The two lowest singlet states, which govern the properties at low temperatures, are nearly degenerate. The right part of Fig. 6 pictures the calculated orbital wave function for these two levels.

B. Hamiltonian

In a first approximation, the complete lifting of the degeneracy of the $4f$ ground-state multiplet prohibits the onset of ordering of the corresponding local moments. Previous work,[5] however, has shown that nonzero dipolar matrix elements between the singlets and an exchange interaction exceeding a critical value may lead to so-called induced-moment ordering. In most cases, such transitions were found to be of second order, but more detailed studies revealed that a coupling between $4f$ quadrupoles may provoke first-order magnetic transitions.[19] For the interpretation of our data, we therefore consider a Hamiltonian of the form

$$\mathcal{H}_{tot} = \mathcal{H}_{CEF} + \mathcal{H}_Z + \mathcal{H}_{magn} + \mathcal{H}_{quad}. \tag{6}$$

$\mathcal{H}_{CEF}$ was discussed above in Sec. IV A. The term

$$\mathcal{H}_Z = -g\mu_B \vec{H}_{ext} \vec{J}, \tag{7}$$

with the Landé factor $g=4/5$, represents the Zeeman interaction, which is proportional to the applied field $\vec{H}$ and the total angular momentum $\vec{J}$. The coupling of the dipolar magnetic moments is provided by the exchange coupling via the conduction electrons—i.e., the Ruderman-Kittel-Kasuya-Yosida (RKKY) interaction. The contribution $\mathcal{H}_{magn}$ for the interaction between the magnetic moments on the Pr ions is written as

$$\mathcal{H}_{magn} = -g\mu_B \sum_{j\neq i} A_{i,j} \vec{J}_i \cdot \vec{J}_j, \tag{8}$$

with the exchange integral $A_{i,j}$.

The effective quadrupole-quadrupole interaction is important because it couples the wave functions of the lowest two crystal-field levels. These consist of linear combinations of orbitals with azimuthal quantum numbers $m_J=0, \pm 2, \pm 4$. The relevant Stevens operators are therefore O_2^0 and O_2^2. Since the coupling energy is small in comparison with $k_B T_C$ and in order to avoid the introduction of yet another fit parameter, we shall ignore the deviations of the electric field gradient at the rare-earth site from cylindrical symmetry around the local z axis and approximate the quadrupole-quadrupole interaction by its m_J-diagonal component

$$\mathcal{H}_{quad} = \sum_{i\neq j} K_{i,j} O_2^0(i) O_2^0(j). \tag{9}$$

Mean-field approach

We consider the molecular fields at the site Pr-1 in Fig. 5(b) The transformation $z \rightarrow -z$ transforms Pr-1 into Pr-3. Hence, the magnetization at site 3, $\vec{M}_3$, can be expressed in the coordinates of $\vec{M}_1$ as

$$\vec{M}_3 = (M_3^x, M_3^y, M_3^z) = (M_1^x, M_1^y, -M_1^z). \tag{10}$$

Analogous arguments can be used to express $\vec{M}_2$, $\vec{M}_4$, and $\vec{M}_5$ in components of $\vec{M}_1$. The Pr ions located above and below Pr-1, denoted as Pr-t and Pr-b, each possess a magnetic moment with the same spatial orientation as the one of Pr-1. Assuming an isotropic exchange A_p in the plane and A_c along the Pr chains, the total dipolar interaction is given by

$$\mathcal{H}_{mag} = -g\mu_B A_p (\vec{J}_1\vec{J}_2 + \vec{J}_1\vec{J}_3 + \vec{J}_1\vec{J}_4 + \vec{J}_1\vec{J}_5) - g\mu_B A_c (\vec{J}_1\vec{J}_t + \vec{J}_1\vec{J}_b). \tag{11}$$

The mean-field approximation leads to

$$\mathcal{H}_{mf} = -2g\mu_B A_p \vec{J}(\langle J^x\rangle, 5\langle J^y\rangle, -\langle J^z\rangle) - 2g\mu_B A_c(\langle J^x\rangle, \langle J^y\rangle, \langle J^z\rangle), \tag{12}$$

where $\langle J^\nu\rangle$ is the thermal average of the νth angular momentum component. Similarly, the quadrupole-quadrupole interaction is transformed into

$$\mathcal{H}_{quad}^{mf} = K\langle O_2^0\rangle O_2^0. \tag{13}$$

At this level of approximation, K is an effective coupling constant which also accounts for possible magnetoelastic effects.[20]

In summary, the interaction affecting the Pr ions in PrB_4 is modeled by an effective single-ion Hamiltonian $\mathcal{H}$:

$$\mathcal{H}_{tot} = \sum_{l,m} B_{l,m}\mathcal{O}_l^m - g\mu_B H_{ext}^y J^y + K\langle O_2^0\rangle O_2^0 - g\mu_B A_p \vec{J}(\langle J^x\rangle, 5\langle J^y\rangle, -\langle J^z\rangle) - 2g\mu_B A_c(\langle J^x\rangle, \langle J^y\rangle, \langle J^z\rangle). \tag{14}$$

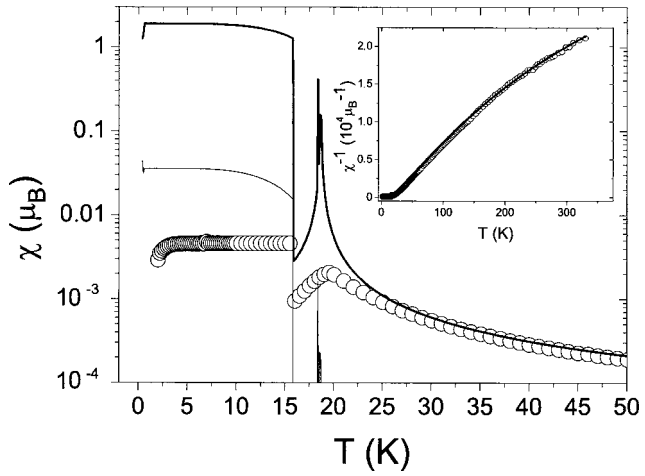

FIG. 7. $\chi_\parallel(T)$ measured for $H=50$ Oe (open circles) and calculated for $H=10$ Oe (thick solid line) for PrB_4. The thin solid line represents the calculated $\chi_\perp(T)$. In the inset we display $\chi_\parallel^{-1}(T)$; the open circles represent the measured values and the solid line results from the calculations.

V. COMPARISON WITH EXPERIMENT AND DISCUSSION

The diagonalization of $\mathcal{H}$ for some given value of $\langle\vec{J}\rangle$ (in three space directions) yields the eigenvalues ϵ_ν and the eigenstates $|\Gamma_\nu\rangle$ of the split $4f$ ground-state multiplet. In turn, the expectation value of the angular momentum,

$$\langle\vec{J}\rangle = \sum_\nu e^{-\epsilon_\nu/k_B T}\langle\Gamma_\nu|\vec{J}|\Gamma_\nu\rangle/Z_{eff}, \tag{15}$$

and of the quadrupolar order parameter,

$$Q = \sum_\nu e^{-\epsilon_\nu/k_B T}\langle\Gamma_\nu|O_2^0|\Gamma_\nu\rangle/Z_{eff}, \tag{16}$$

are obtained with an effective partition function

$$Z_{eff} = \sum_\nu e^{-\epsilon_\nu/k_B T}. \tag{17}$$

Equations (14)–(16) have to be solved self-consistently. Since the crystal-field term H_{CEF} is free of any chosen parameter, the only remaining free parameters are A_p, A_c, and K. By optimizing the parameters to fit the susceptibility and specific-heat data, we find

$$A_p = -3.25 \text{ T}, \quad A_c = 16.2 \text{ T}, \quad K/k_B = -0.33 \text{ K}; \tag{18}$$

i.e., the spins couple ferromagnetically along the c axis and antiferromagnetically in the plane. Mainly due to the strong crystalline anisotropy, the magnetic exchange constant A_c along the Pr chains is 5 times stronger than A_p. In Fig. 7, we plot the measured (open circles) and the calculated (thick solid line) $\chi_\parallel(T)$ of PrB_4. The thick solid line represents the calculation for a single magnetic ion. At $T<T_C$, the magnetic

moment of a single ion or a domain adopts its expected maximum value. However at low fields, demagnetization and domain effects, as indicated by the hysteresis in Fig. 3, may result in a substantially reduced value of the measured magnetization. Nevertheless, the calculation reproduces the ferromagnetic ground state with a saturation magnetization $\mu_{sat} \sim 1.9\mu_B$/(Pr ion) and, with respect to the experiment, a slightly reduced Curie temperature $T_C^{calc} \approx 15.5$ K. The thin solid line in Fig. 7 shows the calculated in-plane susceptibility. The calculated anisotropy ratio $\chi_\parallel \chi_\perp$ is ≈ 60 at $T < T_C$. Upon enhancing the temperature, the quadrupole-quadrupole interaction causes a first-order transition at T_C^{calc} from the ferromagnetic to an antiferromagnetic phase. If K is reduced, both phase transitions shift to higher temperatures. However, considering a purely magnetic interaction and attempting a satisfactory agreement with $\chi(T)$ from experiment leads neither to a first-order phase transition nor to a level splitting consistent with the experimental results for $C_p(T)$ at $T < 15$ K. We recall that antiferromagnetic order is the usual type of ordering in the tetraboride series. Whereas for TbB_4 the spins order in the plane,[21] ErB_4 adopts a configuration with $\vec{J} \| \vec{c}$.[22] The large anisotropy observed in the present $\chi(T)$ experiments, which is well reproduced by the calculations, and the shape of $\chi_\parallel(T)$ close to T_N at low field strongly suggest a moment configuration similar to that in ErB_4. However, we cannot distinguish between the three moment alignments with $\vec{J} \| \vec{c}$ that were identified for the antiferromagnetic order in the tetraborides.[22]

The two phases adopt energies of

$$\langle E^{(f,af)} \rangle = \sum_\nu e^{-\epsilon_\nu^{(f,af)}/k_B T} \epsilon_\nu^{(f,af)} / Z_{eff}^{(f,af)}. \tag{19}$$

Since the respective values of $\langle E \rangle / k_B$ differ by less than 1 K at temperatures around T_C, the calculation is particularly tedious between 13 and 23 K. At T_C^{calc}, the calculated expectation values $\langle \vec{J} \rangle$ and Q (see top panel of Fig. 8) exhibit a discontinuity. In the lower panel of Fig. 8, we plot the temperature-dependent gap between the lowest two singlets as $\Delta_1(T) = \epsilon_2(T) - \epsilon_1(T)$ between 0.5 and 50 K. The small anomaly appearing at T_N is due to computational difficulties, caused by the near degeneracy of the ferromagnetic and antiferromagnetic configurations of the ordered moments. By comparing the left part of Fig. 6 with the lower panel of Fig. 8, we note that the interactions considerably enhance the CEF splitting of the singlet energy levels. The onset of ferromagnetism enhances the separation of the two lowest singlets even further. Previous experiments revealed that the onset of ferromagnetism is coupled to a distortion of the lattice parameter a by less than 0.1%.[3] This effect, also observed in other tetraborides which order antiferromagnetically, is taken into account in our effective quadrupole-quadrupole coupling constant K.

The eigenvalues $\epsilon_\nu(T)$ may now be inserted into the formula for calculating the specific heat due to excitations within the CEF-split $4f$-electron energy-level scheme,[17]

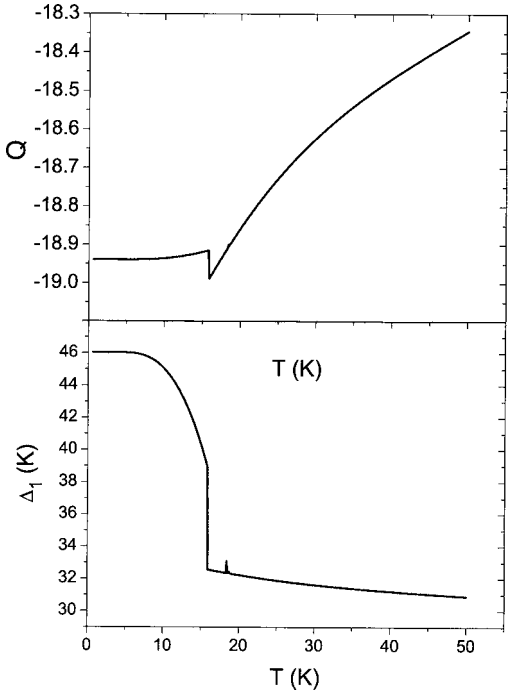

FIG. 8. The upper panel displays the expectation value $Q = \langle O_2^0 \rangle$ for the quadrupolar operator for temperatures between 0.4 and 50 K. In the lower panel, the splitting of the lowest two CEF levels is plotted for the same temperature range.

$$\frac{C_{CEF}}{R}(T) = T \frac{\partial^2}{\partial T^2}[T \ln(Z_{eff})] = \frac{1}{Z_{eff}} \sum_\nu e^{-\epsilon_\nu / k_B T} \left[\left(\frac{\epsilon_\nu}{k_B T} \right)^2 - \frac{\epsilon_\nu \epsilon_\nu'}{k_B^2 T} \right] - \frac{1}{Z_{eff}^2} \left(\sum_\nu e^{-\epsilon_\nu / k_B T} \frac{\epsilon_\nu}{k_B T} \right)^2, \tag{20}$$

where R is the ideal-gas constant and ϵ_ν' is the temperature derivative of the energy eigenvalues ϵ_ν. The $C_p(T)$ data shown in Fig. 4 suggest that for $T < 4$ K, the specific heat is dominated by the contribution due to the hyperfine-split energy levels of the ^{141}Pr nuclei,

$$\frac{C_{nuc}}{R}(T) = \frac{1}{Z_{nuc}} \sum_{j=1}^{2I+1} \left(\frac{\Delta_H j}{k_B T} \right)^2 \exp\left(- \frac{\Delta_H j}{k_B T} \right) - \left[\sum_{j=1}^{2I+1} \frac{\Delta_H j}{k_B T} \exp\left(- \frac{\Delta_H j}{k_B T} \right) \right]^2 \Bigg/ Z_{nuc}^2, \tag{21}$$

with

$$Z_{nuc} = \sum_{j=1}^{2I+1} \exp\left(- \frac{\Delta_H j}{k_B T} \right) \tag{22}$$

and the hyperfine level splitting

$$\Delta_H = \frac{\mu_n H_{hf}}{I}. \tag{23}$$

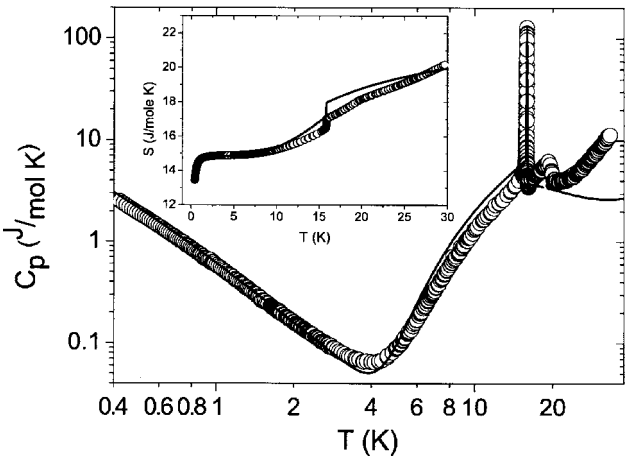

FIG. 9. The measured specific heat $C_p(T)$ (open circles) in zero magnetic field. The solid line represents the result of the calculations explained in the text. The inset shows the entropies, as they follow from experiment (open circles) and model calculations (solid line).

Praseodymium naturally occurs as ^{141}Pr with an abundance of nearly 100%. For ^{141}Pr, the nuclear spin I, the nuclear magnetic moment μ_n, and the hyperfine field H_{hf} are[23]

$$I = 5/2,$$

$$\mu_n = 4.28\mu_N,$$

$$H_{hf} \approx 300 \text{ T}, \tag{24}$$

where μ_N is the nuclear magneton. As may be seen, with the parameters obtained independently from ^{141}Pr NMR experiments,[23] the measured specific heat is reproduced very well.

$C_{CEF}(T)$ for 5 K$<T<$15 K is controlled by $\Delta_1(T)$; the contributions of all other levels at higher energies are negligible. In Fig. 9, we display the measured total specific heat $C_p(T)$ as open circles for 0.4 K$<T<$30 K in a double-logarithmic plot. The solid line represents the calculated $C_{mag}=C_{CEF}(T)+C_{nuc}(T)$. The good agreement between calculated and measured curves confirms the validity of the magnetization-dependent CEF level scheme obtained from the fit to the susceptibility. Despite the fact that the calculation yields a first-order transition at $T_C=15.5$ K, the features of the calculated specific heat are of limited reliability near T_C, as usual in applications of mean-field theory. However, it is rewarding that the calculation yields nearly the observed values for the Curie temperature T_C and for the discontinuity in the entropy (see the inset of Fig. 9). At temperatures above 15 K, the phonon specific heat C_{latt} is no longer small compared to the magnetic specific heat C_{mag} as can be inferred from Refs. 24 and 25. The electronic band-structure calculation yields a density of states at the Fermi level in ferromagnetic PrB_4 of $D(E_F)=241$ states/(cell hartree) and a coefficient $\gamma=5.2$ mJ/(mol K^2) for the specific heat due to conduction electrons, indicating that this contribution is small even in the range of the minimum of $C_p(T)$ shown in Fig. 9. No attempt was made to calculate C_{latt}.

TABLE II. Most important numerical results on PrB_4.

Property	Value
μ_n	$4.28\mu_N$
H_{hf}	300 T
I	5/2
$\langle r^2\rangle$	$1.45a_B^2$
$\langle r^4\rangle$	$8.0a_B^4$
$\langle r^6\rangle$	$150a_B^6$
A_p	−3.25 T
A_c	16.2 T
K	−0.33 K
T_C^{meas}	15.9 K
T_C^{calc}	15.5 K
T_N^{meas}	19.5 K
T_N^{calc}	18.7 K
ΔQ	8.6 J/mol

For completeness, we list the principal numerical values of experimental and theoretical parameters in Table II.

VI. CONCLUSION

We have measured the magnetoresistance, the magnetization, and the specific heat of a PrB_4 single crystal and obtained the magnetic phase diagram in zero field. PrB_4 undergoes a second-order transition into an antiferromagnetic state at $T_N=19.5$ K. However, below $T_C=15.9$ K, the ferromagnetic state is energetically more stable down to the lowest temperatures. The transition from the antiferromagnetic to the ferromagnetic state is of first order, displaying hysteresis and a latent heat $\Delta Q=8.6$ J/mol. The sharp transition indicates that critical fluctuations are almost completely absent.

The temperature dependence of the magnetic moment and the specific heat can be explained by a self-consistent mean-field calculation employing all $4f$ levels split by the CEF. Besides the Zeeman term, an anisotropic magnetic exchange and an effective ferroquadrupolar coupling with $K/k_B=-0.33$ K are included in the calculation. In order to reproduce the experimental $\chi(T)$ data, the Pr ions along the crystal c axis have to be coupled ferromagnetically and those in the ab plane antiferromagnetically. The self-consistent calculations reveal the substantial influence of the quadrupole-quadrupole interaction H_{quad} on the magnitude of T_C and the onset of ferromagnetism, as well as on the first-order character of the transition.

Our work confirms previous claims concerning phase transitions in all-singlet systems.[19] The new aspect here is the parameter-free calculation of the CEF splitting of the $4f$-electron ground-state multiplet and the almost perfect agreement between various experimental quantities and calculations which only require the introduction of three additional parameters describing the interaction between the ionic magnetic moments.

The reason for the discrepancy between our experimental observations and previously reported[2,8] data for the same material is still at the level of speculation. We suspect that it is related to the synthesis procedure. Our single-crystalline samples were grown out of a flux with a 3:1 composition of Pr and Co and the amount of PrB_4 was about one-tenth of that of the flux material. We have also grown other crystals of PrB_4 in the same way using a Pr/Ni flux. Only the crystals grown with Co exhibit the first-order transition features that are reported here. As mentioned above the first-order nature of the transition in the model calculation depends critically on the magnitude of K. It is unlikely that small concentrations of Co or Ni impurities in the samples would significantly alter the essential parameters that determine the strength of each term in Eq. (6) and, therefore, the difference in behavior is, most likely, due to not-yet-identified effects of trace defects.

ACKNOWLEDGMENTS

We thank M. Leopold for providing the x-ray diffraction pattern displayed in Fig. 1 and M. Richter for providing the effective charges obtained with the Dresden-FPLO code. One of us (R.M.) gratefully acknowledges enlightening discussions with B. Delley, M. Richter, and M. Kuzmin. This work has benefited from partial financial support of the Schweizerische Nationalfonds zur Förderung der wissenschaftlichen Forschung and NSF Grant No. DMR-0203214.

[1] R. W. Johnson and A. H. Daane, J. Chem. Phys. **38**, 425 (1963).
[2] Z. Fisk, M. B. Maple, D. C. Johnston, and L. D. Woolf, Solid State Commun. **39**, 1189 (1981).
[3] A. Berrada, J. P. Mercurio, B. Chevalier, J. Etourneau, P. Hagenmuller, M. Lalanne, J. C. Gianduzzo, and R. Georges, Mater. Res. Bull. **11**, 1519 (1976).
[4] G. T. Trammell, Phys. Rev. **131**, 932 (1960).
[5] B. Bleaney, Proc. R. Soc. London, Ser. A **276**, 19 (1963).
[6] B. R. Cooper, Phys. Rev. **163**, 444 (1967).
[7] K. H. J. Buschow and J. H. N. Creighton, J. Chem. Phys. **64**, 1994 (1976).
[8] J. Etourneau, J. P. Mercurio, A. Berrada, P. Hagenmuller, R. Georges, R. Bourezg, and J. C. Gianduzzo, J. Less-Common Met. **67**, 531 (1979).
[9] We thank E. Moshopoulou for the x-ray structure verification.
[10] A. Zalkin and D. H. Templeton, Acta Crystallogr. **6**, 629 (1953).
[11] J. C. Gianduzzo, R. Georges, B. Chevalier, J. Etourneau, P. Hagenmuller, G. Will, and W. Schäfer, J. Less-Common Met. **82**, 29 (1981).
[12] W. N. Lipscomb and D. Britton, J. Chem. Phys. **33**, 275 (1960).
[13] M. Kasaya, K. Takegahara, A. Yanase, and T. Kasuya, *Crystalline Electric Fields Effects in f-Electron Magnetism* (Plenum, New York, 1982), p. 95.
[14] The calculations used the DNP basis set [B. Delley, J. Chem. Phys. **92**, 508 (1990); **113**, 7756 (2000)]. This basis set includes numerical atomic response functions of s, p, d (and f for Pr) character, in addition to the exact numerical solutions for the density functional atom, and is expected to give better than 1 mhartree total accuracy per atom in general. The basis functions have finite tails to help linear scaling methods for all except obtaining the density matrix by diagonalization. Tail lengths were 8 a.u. in these calculations, which is a conservative choice with regards to accuracy. $\vec{k}$-space integrations have been performed with an unshifted $2\times2\times4$ mesh, which amounts to nine symmetry-unique $\vec{k}$ points. A thermal broadening of 5 mhartree has been used. The total energy has been modified with the entropy term proposed by M. Weinert and J. W. Davenport, [Phys. Rev. B **45**, 13709 (1992)] to make the energy functional variational.
[15] Mulliken charges depend on the choice of localized basis functions on which the Bloch functions are projected. Results kindly provided by M. Richter using the FPLO (full-potential local-orbital) method, which uses a different local basis, are consistent with ours. The main message is that the effective charges differ vastly from the nominal valence of the ions.
[16] K. N. R. Taylor and M. I. Darby, *Physics of Rare Earth Solids* (Chapman and Hall, London, 1972).
[17] Z. Liu, M. Richter, M. Diviš, and H. Eschrig, Phys. Rev. B **60**, 7981 (1999). Note that the values of $\langle r^l \rangle$ depend on the environment of the rare-earth ion. Here, we assume that this dependence is weak in metallic praseodymium compounds.
[18] K. W. H. Stevens, Proc. Phys. Soc. London **65**, 14 (1951).
[19] J. Kötzler, G. Raffius, A. Loidl, and C. M. E. Zeyen, Z. Phys. B: Condens. Matter **35**, 125 (1979).
[20] P. Morin and D. Schmitt, Phys. Rev. B **23**, 5936 (1981).
[21] F. Elf, W. Schäfer, G. Will, and J. Etourneau, Solid State Commun. **40**, 579 (1981).
[22] W. Schäfer, G. Will, and K. H. J. Buschow, J. Magn. Magn. Mater. **3**, 61 (1976).
[23] K. Shimizu and K. Ichinose, Solid State Commun. **94**, 619 (1995).
[24] A. S. Bolgar, V. B. Muratov, K. A. Meleshevich, and O. T. Khorpyakov, Sov. Powder Metall. Met. Ceram **29**, 917 (1990).
[25] R. M. Swift and D. White, J. Am. Chem. Soc. **79**, 3641 (1957).